A New Hybrid Method for Magnetic Field Calculation in IPMSM Accounting for Any Rotor Configuration

Guo, Baocheng; Huang, Yunkai; Peng, Fei; Dong, Jianning

DOI
10.1109/TIE.2018.2868252

Publication date
2019

Document Version
Final published version

Published in
IEEE Transactions on Industrial Electronics

Citation (APA)
Guo, B., Huang, Y., Peng, F., & Dong, J. (2019). A New Hybrid Method for Magnetic Field Calculation in IPMSM Accounting for Any Rotor Configuration. *IEEE Transactions on Industrial Electronics*, *66*(7), 5015-5024. Article 8458371. https://doi.org/10.1109/TIE.2018.2868252

A New Hybrid Method for Magnetic Field Calculation in IPMSM Accounting for Any Rotor Configuration

Baocheng Guo, *Member, IEEE*, Yunkai Huang, Fei Peng, *Member, IEEE*,
and Jianning Dong, *Member, IEEE*

***Abstract*—In this paper, a new hybrid model is proposed for the prediction of air gap magnetic field distribution (MFD) in interior permanent magnet machines with any rotor configuration. The slotless magnetic field is first predicted by finite-element method (FEM) with automatic scripting in MATLAB to consider saturation in the rotor iron. Afterward, the conformal mapping viz., Schwarz–Christoffel mapping is introduced to take the slotting effect into account. Consequently, the MFD could be calculated. The back electromagnetic forces, cogging torque, and output torque are obtained accordingly. Then a subdomain model is developed to consider the armature reaction. The results show that the proposed hybrid approach agrees well with the FEM. The model is further verified by experiments. The main contribution of this paper is to reduce the computation time remarkably while maintaining the calculation accuracy.**

***Index Terms*—Finite-element (FE) model, hybrid model, interior permanent magnet (IPM) machines, Schwarz–Christoffel (SC) mapping.**

I. INTRODUCTION

INTERIOR permanent magnet (IPM) machines, due to their high efficiency, high power density as well as wide constant power speed range, are widely used in industrial [1] and home applications, especially in electric vehicles [2]. For both the spoke-type permanent magnet machines and any other IPM with different topologies, their design and optimization are of great importance. However, the considerable long computation time is still remaining as one of the major problems for IPM motor designers because of the complex rotor configuration.

A significant amount of work has been done concerning the design for IPM. At present, the numerical approach, such as finite-element method (FEM), is widely used in motor design since it is regarded as the most accurate method. It is able to consider both saturation and complex geometries. For example, Liu *et al.* studied the performance of the IPM machine used for electric vehicles using FEM [3], while Shin *et al.* performed a similar study in [4]. An alternative method to reduce the computation time is the field reconstruction (FR) method proposed in [5], which is partly based on the FEM model. In [6], the author adopted the FR approach to study the electromagnetic vibrations. Although it is much faster than three-dimensional/two-dimensional (3-D/2-D) finite-element (FE) models, it still requires considerable computation time. Moreover, the optimization of IPM needs large number of iterations to vary geometry dimensions, which takes more time [7].

Analytical or semianalytical approaches, due to their fast and acceptable accuracy, are still regarded as efficient and favorable methods among electrical machine designers.

The magnetic equivalent circuit (MEC) method [8], [9] can calculate the average magnetic field but not the detailed distribution. Moreover, the MEC is not accurate enough for some qualities such as cogging torque and forces because the accuracy is largely affected by the number of nodes and the simulation strategy. In addition, the model needs to be rearranged at each simulation step due to the variations of stator and rotor reluctances.

Alternative analytical solutions are appearing in the literature [10], which is based on the solution of Poisson's and Laplace's equations. In [11], the air gap magnetic field distribution (MFD) of a spoke-type motor is calculated by a subdomain model with assumptions of iron relative permeability with linear equations, which limits the application of the method. In [12], the iterative technique is adopted to consider the permeability, but the model is not applicable to complex rotor structures.

Most general approaches are combining with MEC model to consider the leakage flux [13]–[15] for specific structure. None of the previous studies provide simple and general solutions for MFD of IPM machines. To overcome the aforementioned problems, a hybrid analytical model is proposed to predict the MFD and performance.

A flowchart describing the proposed approach is shown in Fig. 1. It shows that FE model is introduced to obtain the slotless magnetic field, and it should be noted that the FE model

Manuscript received February 2, 2018; revised April 17, 2018; accepted August 17, 2018. Date of publication September 10, 2018; date of current version February 28, 2019. This work was supported in part by the National Nature Science Foundation of China Project 51777034 and in part by the Qing Lan Project. *(Corresponding author: Baocheng Guo.)*

B. Guo, Y. Huang, and F. Peng are with the School of Electrical Engineering, Southeast University, Nanjing 210018, China (e-mail: guobaocheng1986@gmail.com; huangyk@seu.edu.cn; pengfei@seu.edu.cn).

J. Dong is with the Department of Electrical Sustainable Energy, Delft University of Technology, 2628DC Delft, The Netherlands (e-mail: j.dong-4@tudelft.nl).

Color versions of one or more of the figures in this paper are available online at http://ieeexplore.ieee.org.

Digital Object Identifier 10.1109/TIE.2018.2868252

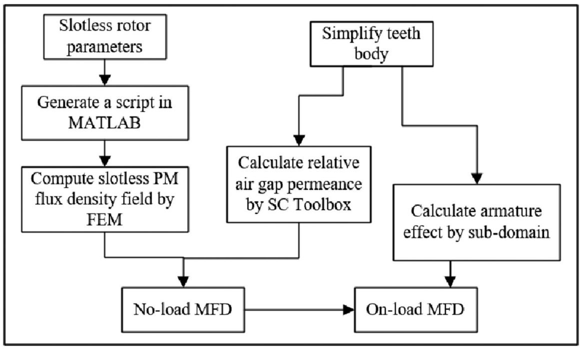

Fig. 1. Flowchart of the hybrid method.

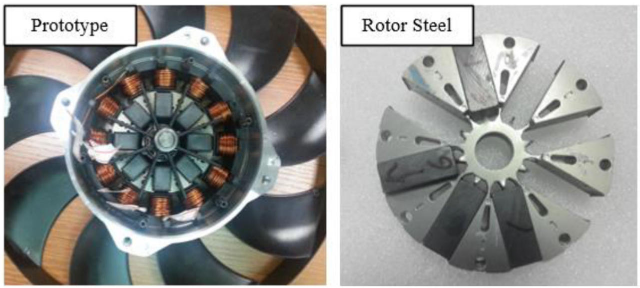

(a) (b)

Fig. 2. Prototype of the IPM electrical machines for fan blower. (a) Prototype. (b) Configuration of rotor.

is used only once; moreover, it is simplified since it no longer needs to consider the slot. After introducing the SC mapping and subdomain, the dynamic magnetic performance can be calculated. This technique can reduce the computation time and maintain the accuracy.

This paper is organized as follows. In Section II, the parameters of prototype are provided. Section III introduces the automatic modeling of FE model. The slotting effect is considered by Schwarz–Christoffel (SC) mapping and the armature reaction is presented in Section IV. Afterward, the results are then discussed in Section V. In Section VI, the experimental results are presented and compared with the results obtained from the proposed hybrid approach. Conclusions are drawn in Section VII.

II. DESCRIPTION OF PROTOTYPE

In this paper, a 12-slot/8-pole spoke-type IPM is introduced to verify the proposed method. The machine has 12-slots stator with a concentered winding, and four-pole pairs spoke-type permanent magnet rotor. The major design objectives are as follows: high efficiency; high thermal endurance; reasonable rotor mechanical behavior; and low cost. The main dimensions and parameters of the studied machine are shown in Table I.

The prototype and its components are shown in Fig. 2. In order to decrease the cost and the PM eddy current loss, the ferrite PMs are adopted. Fig. 3 shows the detailed geometry with rectangle magnets and magnetic bridges.

TABLE I
MAIN DIMENSIONS AND PARAMETERS OF THE STUDIED MACHINE

Symbol	Quantity	Value and unit
P	Number of pole pairs	4
Q	Number of slots	12
N_c	Number of turns per slot	14
L	Length of the rotor and stator	14.5 mm
I	RMS rated current	10A
n_s	Rated speed	3000 rpm
g	Length of air gap	1 mm
Br	Remanence of magnet	0.47 T
	Magnet Type	Ferrite

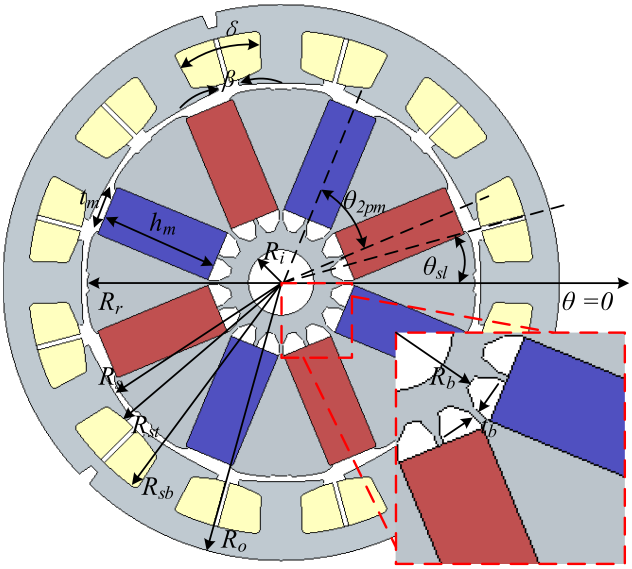

Fig. 3. Configuration of a 12-slot/8-pole spoke-type motor.

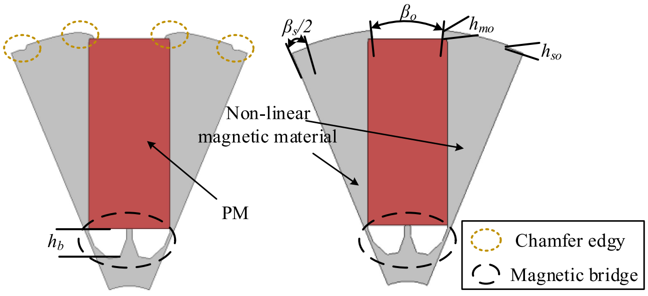

(a) (b)

Fig. 4. Geometry of rotor models. (a) Initial model. (b) Simplified model.

III. AUTOMATIC GENERATION OF SLOTLESS FEM MODEL

A. Simplification of Rotor Structure

Fig. 4(a) shows the initial configuration of rotor geometry. In the aspect of design, the linkage fluxes pass the magnetic bridges resulting in saturation, which makes the permeability distribution uniform. In the meanwhile, the linkage flux makes the magnetic flux density decreased. Hence, the top magnetic bridge is always thin to limit the leakage, and the bottom is thick

TABLE II
CALCULATED SIMPLIFIED DIMENSIONS OF ROTOR STRUCTURE

Symbol	Quantity	Value and unit
R_i	Radius of shaft	7 mm
R_b	Radius of inner bridge	11 mm
t_b	Width of magnetic bridge	0.8 mm
h_b	Height of magnetic bridge	4 mm
h_m	Height of PM	25.5 mm
t_m	Width of PM	10.9 mm
β_o	Width angle of bayonet	13.6°
h_{mo}	Height of bayonet	1.15 mm
β_o	Width angle of side groove	6.6°
h_{so}	Height of side bayonet	3.3 mm
R_r	Radius of outer rotor	41.65 mm

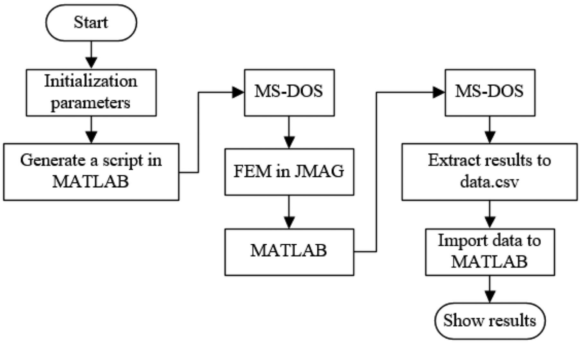

Fig. 5. Data communication between MATLAB and JMAG.

to ensure the mechanical stress. This phenomenon is difficult to be considered in the pure analytical model. However, it can be calculated from an FEM model directly. Therefore, the magnetic bridge area is not simplified.

The rotor chamfer edge is simplified as a rectangle shape as shown in Fig. 4(b). By doing the simplification, the geometry can be easily parametrized, which is good for further optimization.

The dimensions of the simplified rotor structure are shown in Table II.

B. Automatic FEM Modeling Using MATLAB and JMAG-Designer

To speed up the modeling process, a user interface is built between the FEM model and MATLAB. JMAG-Designer is used as the FEM tool.

Fig. 5 shows the process of automatic modeling, which also illustrates the interfaces between MATLAB and JMAG. Different scripts are used for functionalities from preprocessing to postprocessing. The scripts are generated in MATLAB dynamically based on previous inputs. It should be noted that any rotor topologies could be calculated based on this approach.

To speed up the calculation, a 1/8 slotless model is adopted, and the stator is replaced with a slotless cylinder, as shown in Fig. 6. The antiperiodic boundary condition is set on both sides, the FE model has 8193 elements and is calculated under static analysis. Since the nonlinear magnetic material is used in the FE model, the saturation of the bridge can be directly considered without manual iterative process. It can be seen that the magnetic flux density at bridge area is 2.4 T.

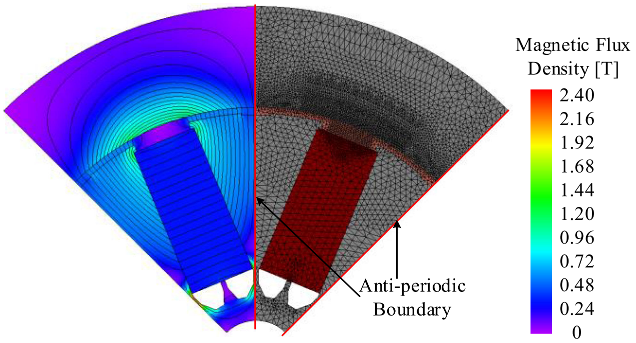

Fig. 6. Magnetic flux density and meshing of prototype.

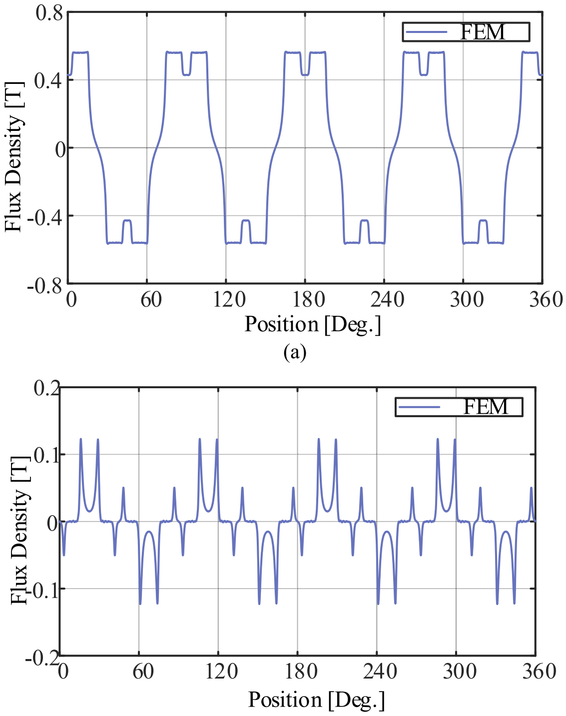

(a)

(b)

Fig. 7. Slotless air gap flux density waveforms of FE model. (a) Radial component. (b) Tangential component.

Afterward, the flux density can be extracted from FEM software to a text file (*.csv) and imported to MATLAB. Fig. 7 shows the no-load air gap flux density waveforms of FE model.

IV. SLOTTING EFFECT AND ARMATURE REACTION

In order to simplify the calculation, the tooth body has uniform width [see Fig. 8(a)] is simplified to the one has equal width angle as shown in Fig. 8(b). It should be noted that this simplified structure should fulfill the standard boundary conditions of Poisson's and Laplace's equations, which is used to calculate the relative air gap permeance and armature reaction.

The simplified parameters of stator structure, which are used to calculate the relative air gap permeance and armature reaction, are shown in Table III.

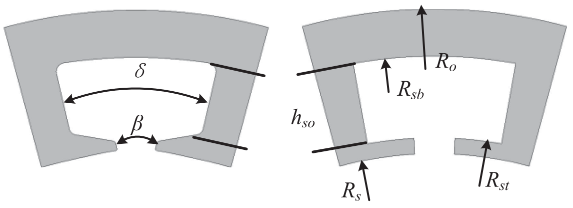

(a) (b)

Fig. 8. Geometry of stator models. (a) Initial model. (b) Simplified model.

TABLE III
CALCULATED SIMPLIFIED PARAMETERS OF STATOR STRUCTURE

Symbol	Quantity	Value and unit
R_s	Radius of inner stator	42.65 mm
R_{st}	Radius of slot top	44.5 mm
R_{sb}	Radius of slot bottom	54 mm
R_o	Radius of outer stator	59.5 mm
β	Slot opening width angle	5.8°
δ	Slot width angle	20.22 °

A. Complex Relative Air Gap Permeance

There are several approaches which consider the slotting effect shown in [16] viz., lateral force (LF) and complex permeance (CP) techniques. Although LF is convenient and fast, it cannot predict the tangential component, for which the accuracy of torque is not good enough.

The conformal mapping (CM) adopted in [16] is one of the CP methods and always used to calculate the relative air gap permeance to obtain the air gap magnetic field with slotting based on the slotless results. In [17], Zarko used this method to calculate the relative permeability of the air gap considering the slotting effect, but one of the main assumptions is that the motors have an infinite slot opening, which implies that the shape of slot is ignored. Moreover, the interaction between adjacent slots is also neglected. In this paper, the numerical SC mapping is used with MATLAB SC Toolbox to exempt the previous assumptions [18]. The SC mapping is better than the traditional CM shown in [16], because of its versatility and accuracy.

The complex relative air gap permeance for the slotted air gap can be calculated as

$$\lambda = \frac{\partial \varsigma}{\partial w} \cdot \frac{\partial w}{\partial z} \cdot \frac{\partial z}{\partial s} \cdot \frac{1}{\lambda_0} \tag{1}$$

$$\lambda = \lambda_r + j\lambda_t \tag{2}$$

where λ_0 is the relative permeance in the slotless air gap, λ_r and λ_t stand for the radial and tangential components of the complex relative air gap permeance, respectively. Moreover, s, z, w, and ς represent the s-plane, the z-plane, the w-plane, and the ς-plane, respectively.

To obtain the relative air gap permeance, the points of each domain can be mapped as shown in Fig. 9. First, the modified motor geometry (s-plane) is mapped to the multilateral geometry in the z-plane by using one logarithmic equation as

$$z = \log(s). \tag{3}$$

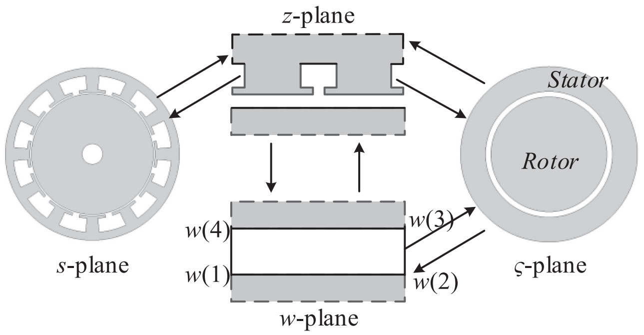

Fig. 9. Illustration of mapping between different domains in SC method.

The canonical rectangle in the w-plane can be mapped to the interior of polygon in the z-plane using the SC mapping as

$$z = f(w) = A_0 + C_0 \int \prod_{k=1}^{n-1} (w - w_k)^{\alpha_k - 1} dw \tag{4}$$

where A_0 and C_0 are the integration constants, n is the number of polygon corners in the z-plane, w presents the points in the canonical rectangle, and α_k are the interior angles. These points and unknown parameters can be calculated by SC Toolbox.

The interior of annular domain in ς-plane is mapped to the canonical rectangle in the w-plane using

$$w = j\left(\log(\varsigma)\frac{\Delta x}{2\pi} + \frac{\Delta y}{2} - j\frac{\Delta x}{2}\right)$$

$$\Delta x = w(2) - w(1),\ \Delta y = w(3) - w(2). \tag{5}$$

After reaching the annular domain, Hague's solution is then used to calculate the slotless air gap field in ς-plane. It should be noted that every mapping function can be inversed. Hence, the CP for slotted air gap is presented by

$$\lambda_1 = \frac{\partial \varsigma}{\partial w} \cdot \frac{\partial w}{\partial z} \cdot \frac{\partial z}{\partial s}. \tag{6}$$

In order to obtain the final relative permeance by (1), the CP under slotless air gap should be calculated by the same procedure, and the radial and tangential components of complex relative permeance in the middle air gap are shown in Fig. 10. It should be noted that in order to obtain accurate results, all slots should be drawn in SC Toolbox to consider the effect of adjacent slots.

Having the slotless air gap flux density (B_u) obtained by FE model, the slotted air gap flux density (B_s) can be calculated using the complex relative air gap permeance

$$B_s = B_u \cdot \lambda = (B_r + jB_t) \cdot (\lambda_r + j\lambda_t) \tag{7}$$

where B_u is the complex conjugate, B_r and B_t are the no-load radial and tangential components, respectively.

It can be seen from previous description that the static FE step is independent from the analytical step. Since complex

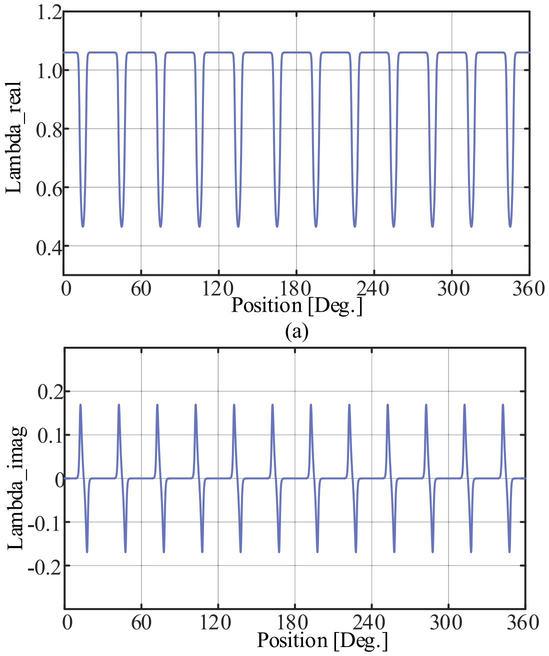

(a)

(b)

Fig. 10. Complex relative permeance in the middle of air gap with 5.8° slot opening. (a) Radial component. (b) Tangential component.

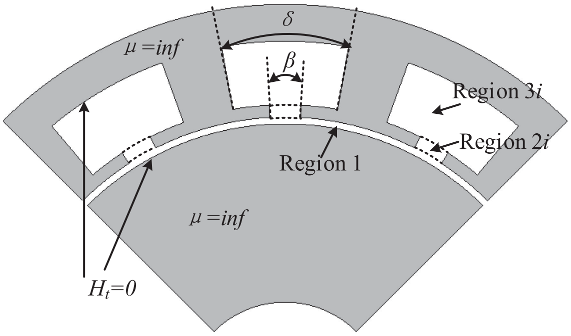

Fig. 11. Exact SD model.

rotor structures can be directly modeled in FEM, the proposed hybrid method can be applied to machines with arbitrary PM rotor structures. After obtaining the no-load field distribution, the armature reaction should be calculated in order to obtain the on-load MFD.

B. Model of Armature Reaction

To take armature reaction into account, the subdomain model is selected since it provides more accurate results. Normally, several assumptions are made to simplify the calculation: 1) the iron materials have infinite permeablity; 2) the end effect is ignored; and 3) simplified slots as shown in Fig. 8(b).

Afterward, the exact SD model can be separated into three domains as shown in Fig. 11 viz., air gap (region 1), winding slot (region 2i), and slot openings (region 3i). The angular position of the ith stator slot-opening is defined as

$$\theta_i = -\frac{\beta}{2} + \frac{2i\pi}{Q},\ 1 \le i \le Q. \tag{8}$$

By using separation of technique, the solution of Poisson and Laplace equations can be obtained. In order to avoid ill-conditioned matrix, the scaling technique is introduced as

$$P_\omega(u,v) = \left(\frac{u}{v}\right)^\omega + \left(\frac{v}{u}\right)^\omega,\ E_\omega(u,v) = \left(\frac{u}{v}\right)^\omega - \left(\frac{v}{u}\right)^\omega. \tag{9}$$

Taking into account the boundary conditions shown in Fig. 11 ($H_t = 0$), the general solution of vector potential A in region 1 (air gap) is simplified as

$$A_I(r,\theta) = \sum_{n=1}^{\infty}\left(A_n^1 \frac{P_n(r,R_r)}{P_n(R_s,R_r)}\right)\cos(n\theta) + \sum_{n=1}^{\infty}\left(C_n^1 \frac{P_n(r,R_r)}{P_n(R_s,R_r)}\right)\sin(n\theta). \tag{10}$$

The general solution of region 2i (slot opening) is

$$A_{2i} = A_0^{2i} + B_0^{2i}\ln r + \sum_{k=1}^{\infty}\left(A_k^{2i}\frac{E_{k\pi/\beta}(r,R_{\mathrm{st}})}{E_{k\pi/\beta}(R_s,R_{\mathrm{st}})} - B_k^{2i}\frac{E_{k\pi/\beta}(r,R_{\mathrm{st}})}{E_{k\pi/\beta}(R_s,R_{\mathrm{st}})}\right) \cdot \cos\left(k\pi(\theta-\theta_i)/\beta\right). \tag{11}$$

The same boundary condition shown in Fig. 11 ($H_t = 0$), the general solution of region 3i (winding slot) can be expressed as

$$A_{3i}(r,\theta) = A_0^{3i} + \frac{1}{2}\mu_0 J_j\left(R_{\mathrm{sb}}^2\ln r - \frac{1}{2}r^2\right) + \sum_{m=1}^{\infty}\left(A_m^{3i}\frac{\delta R_{\mathrm{st}}}{m\pi}\frac{P_{m\pi/\beta}(r,R_{\mathrm{sb}})}{E_{m\pi/\beta}(R_{\mathrm{st}},R_{\mathrm{sb}})}\right) \cdot \cos\left(\frac{m\pi}{\delta}\left(\theta-\theta_i-\frac{1}{2}(\beta-\delta)\right)\right) \tag{12}$$

where A_n^1, C_n^1, A_0^{2i}, B_0^{2i}, A_k^{2i}, B_k^{2i}, A_0^{3i}, and A_m^{3i} are coefficients to be determined. n, k, and m are harmonic order in each computed domain.

It should be noted that each domain is connected by the continue boundary condition. The one between region 1 and region 2i at R_s is

$$A_1(R,\theta) = A_{2i}(R,\theta),\ \theta_i - \frac{\beta}{2} \le \theta \le \theta_i + \frac{\beta}{2} \tag{13}$$

$$\begin{cases} H_{x1}(R,\theta) = H_{x2i}(R,\theta), & \theta_i - \frac{\beta}{2} \le \theta \le \theta_i + \frac{\beta}{2} \\ H_{x1}(R,\theta) = 0, & \text{elsewhere.} \end{cases} \tag{14}$$

The boundary condition between region 2i and region 3i at R_{st} is

$$A_{3i}(R,\theta) = A_{2i}(R,\theta),\quad \theta_i - \frac{\beta}{2} \le \theta \le \theta_i + \frac{\beta}{2} \tag{15}$$

$$\begin{cases} H_{x3i}(R,\theta) = H_{x2i}(R,\theta), & \theta_i - \frac{\beta}{2} \le \theta \le \theta_i + \frac{\beta}{2} \\ H_{2ix}(R,\theta) = 0, & \text{elsewhere.} \end{cases} \tag{16}$$

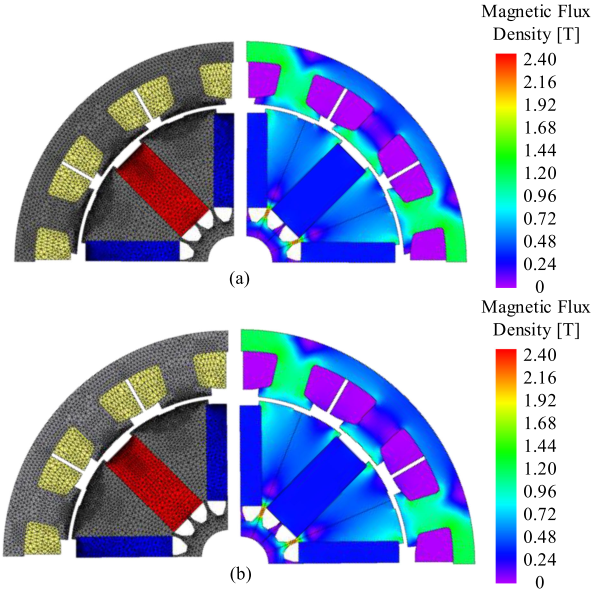

Fig. 12. FE model. (a) Slot opening with 5.8°. (b) Slot opening with 11.6°.

The unknown coefficients can be obtained by applying Fourier series expansion and boundary conditions. The detailed calculation method can be seen in [19].

Afterward, the radial and tangential flux density components are derived from A as shown in the following:

$$B_r = \frac{1}{r}\frac{\partial A}{\partial \theta}, \quad B_t = -\frac{\partial A}{\partial r}. \tag{17}$$

Hence, the on-load flux density distribution could be obtained by superposition principle [20], and it becomes

$$\vec{B}_{\text{on-load}} = \vec{B}_{\text{PM}} + \vec{B}_{\text{AR}} \tag{18}$$

where $\vec{B}_{\text{PM}}$ is the flux density produced by the PMs and $\vec{B}_{\text{AR}}$ is the flux density of the armature reaction.

V. Results and Analysis

The proposed method is verified by 2-D nonlinear FEM model as shown in Fig. 12. In order to validate the proposed method with different stator configurations, an FEM model with a slot opening of 11.6° is also built and considered in the comparison. It should be noted that there are some structural simplifications in the FEM model to verify the results calculated by the proposed method. To speed up the calculation, only one-fourth model is developed and the mesh at the air gap is refined as shown in Fig. 12.

A. No-Load Performance

Fig. 13 compares the flux density in the middle circle of the air gap. It shows that the results predicted by the proposed method agree well with those obtained from the FEM model even with large slot opening.

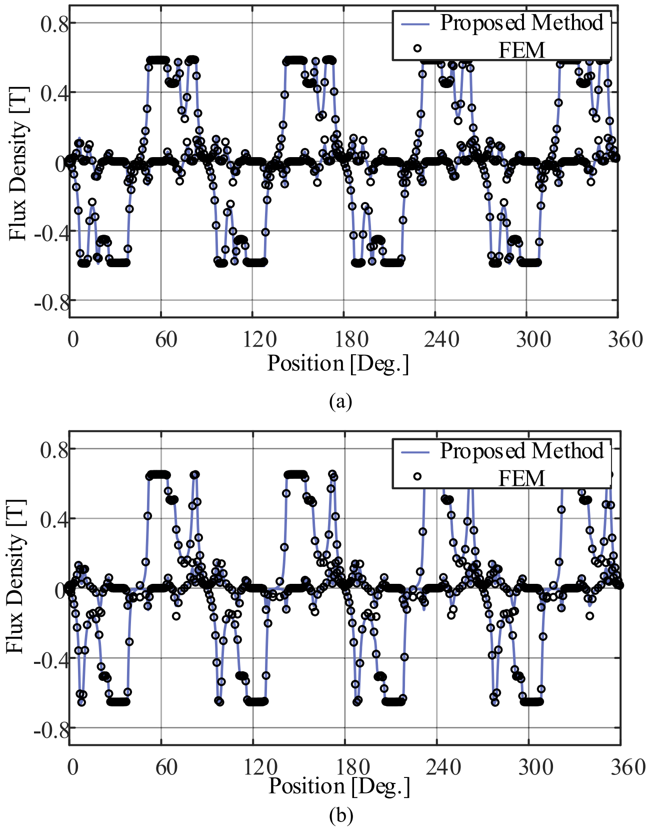

Fig. 13. No-load air gap flux density waveforms of proposed method and FEM. (a) Slot opening with 5.8°. (b) Slot opening with 11.6°.

The phase flux vector can be given by

$$\begin{pmatrix} \Psi_a \\ \Psi_b \\ \Psi_c \end{pmatrix} = N_c\,[C]\,(\varphi_1\,\varphi_2 \ldots \varphi_Q) \tag{19}$$

where N_c is the number of turns in series per phase and [C] is a connecting matrix that illustrates the windings distribution. Under no-load condition, the flux over each slot (φ_j) is

$$\varphi_j = L \cdot \int_{\theta_0}^{\theta_0+\theta_c} B_r(R_a, \theta)d\theta \tag{20}$$

where L is the axial length, θ_0 is the coil starting side angle from the origin, θ_c is the expansion angle of the coil pitch, and R_a is the average radius of air gap.

The connecting matrix C is given by

$$C = \left[\begin{matrix} 1 & -1 & 0 & 1 & -1 & 0 \\ 0 & 1 & -1 & 0 & 1 & -1 \\ -1 & 0 & 1 & -1 & 0 & 1 \end{matrix}\right.$$

$$\left.\begin{matrix} 1 & -1 & 0 & 1 & -1 & 0 \\ 0 & 1 & -1 & 0 & 1 & -1 \\ -1 & 0 & 1 & -1 & 0 & 1 \end{matrix}\right]. \tag{21}$$

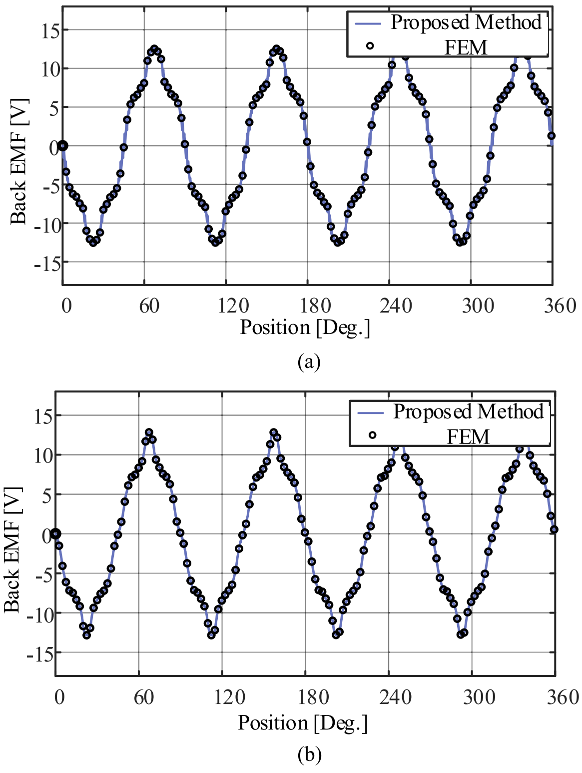

Fig. 14. Comparison of back EMF. (a) Slot opening with 5.8°. (b) Slot opening with 11.6°.

Afterward, the back EMFs are calculated by

$$\begin{pmatrix} E_a \\ E_b \\ E_c \end{pmatrix} = n_s \frac{d}{d\,\triangle} \begin{pmatrix} \Psi_a \\ \Psi_b \\ \Psi_c \end{pmatrix}. \tag{22}$$

The back EMFs are shown in Fig. 14. The computation is done at rated speed 3000 r/min. The results obtained from the proposed method are in agreement with the FEM ones.

According to the Maxwell tensor equation, the torque can be computed by

$$T = \frac{LR_a^2}{\mu_0} \int_0^{2\pi} B_r(R_a, \theta) \cdot B_t(R_a, \theta) d\theta. \tag{23}$$

Fig. 15 shows the cogging torque of prototype. As shown, the proposed method is able to predict the cogging torque with high degree of accuracy for both slot opening.

B. On-Load Permeance

Fig. 16 compares the flux density in the middle air gap. It shows that the results predicted by the proposed method match those from FEM model. It should be noticed that the errors increase compared to those of EMF and cogging torque, which is mainly caused by the simplification of the rotor when calculating the armature effect. More specifically, the groove at the rotor surface is neglected in order to reach the balance between computation time and accuracy.

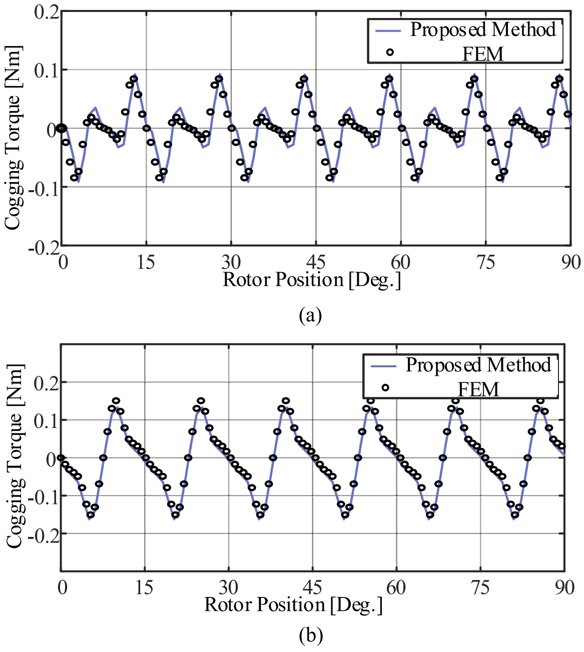

Fig. 15. Comparison of cogging torque. (a) Slot opening with 5.8°. (b) Slot opening with 11.6°.

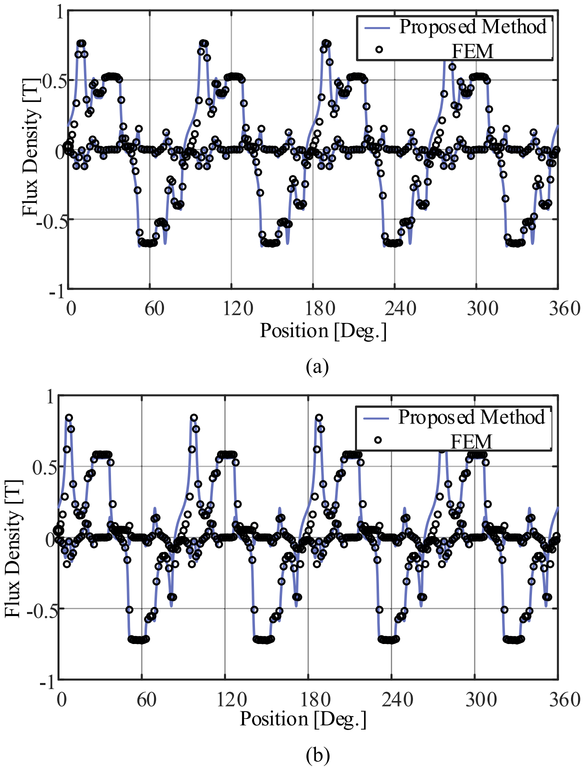

Fig. 16. On-load air gap flux density waveforms of proposed method and FEM. (a) Slot opening with 5.8°. (b) Slot opening with 11.6°.

Fig. 17 shows the electromagnetic torque waveforms calculated by the proposed method and the FEM model under 10 A current. The average value of the hybrid method is 0.50 N·m and that of the FEM is 0.53 N·m for the slot opening of 5.8°.

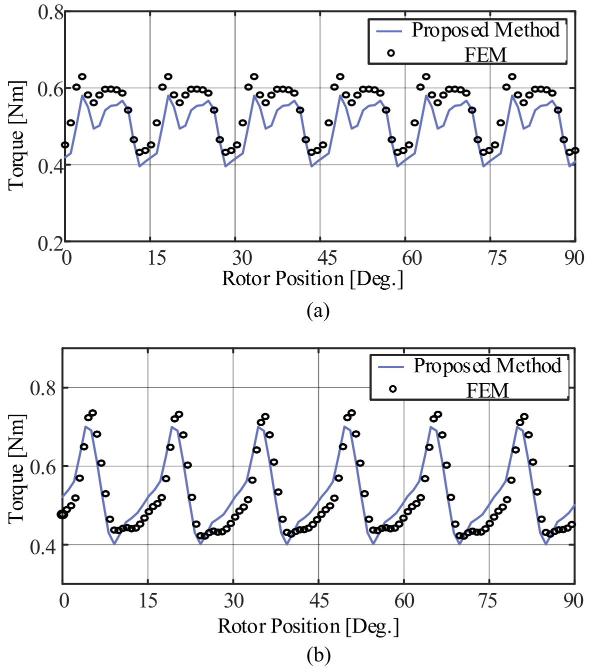

(a)

(b)

Fig. 17. Comparison of torque. (a) Slot opening with 5.8°. (b) Slot opening with 11.6°.

The average value of the hybrid method is 0.536 N·m and that of the FEM is 0.532 N·m for the slot opening of 11.6°. The errors are 6% and 0.7%, respectively, which is in acceptable range. The waveform error is caused by neglecting of rotor grooves and stator local saturation.

C. Computation Time

In terms of the computation time, the FEM model has 11 713 elements and it requires 377 and 817 seconds to obtain the basic no-load and on-load performances [i7-4800 MQ @ 2.70(GHz) CPU, 32 (GB) RAM], respectively. The hybrid method proposed in this paper, on the other hand, require only 13 seconds to get the no-load results and 31 seconds for on-load results. Therefore, the hybrid model is about much faster than FEM.

VI. EXPERIMENTAL VALIDATION

Fig. 18 shows the prototype machine (slot opening of 5.8°) and the experimental set-up and devices. The prototype machine is driven by a driving motor via a shaft coupling.

The no-load EMF is measured at 1200 r/min. The measured waveforms are shown in Fig. 19(b). The calculated results are quite close to the measured ones, as shown in Fig. 19(a).

The rms value of experimental results is 3.1 V, while the value calculated by proposed method is 3.2 V. However, there is a little difference between the waveform shapes obtained from the proposed method and the measured ones. It is mainly caused by the chamfering of the rotor. It results in the difference of the MFD, and this phenomenon is confirmed by Fig. 11. Although the proposed results show certain error with the experiments, the work in this paper is still meaningful since the hybrid model can achieve accurate enough results in a very short time.

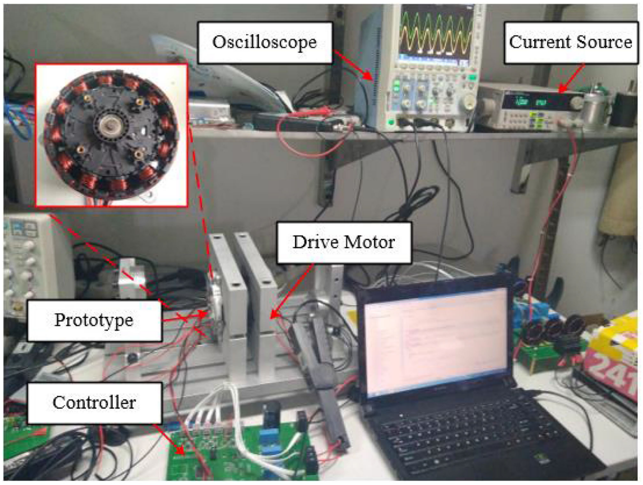

Fig. 18. Prototype machine and the experimental setup.

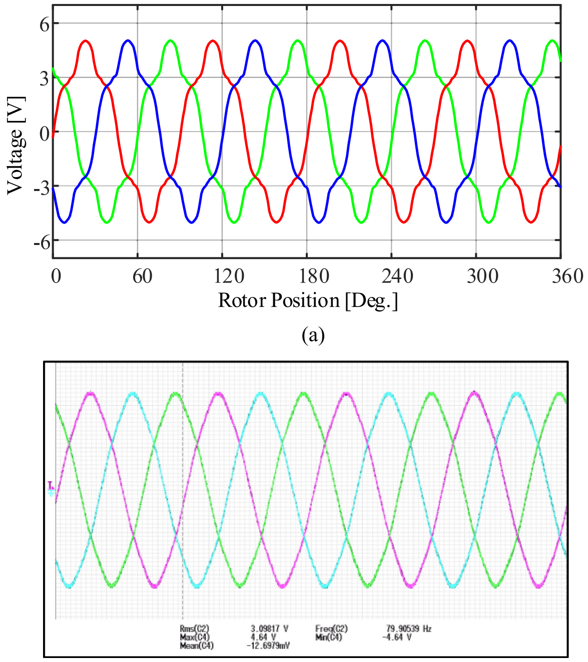

(a)

(b)

Fig. 19. EMF results of slot opening with 5.8°. (a) Calculated result. (b) Experimental result.

The cogging torque is relatively small and it is hard to test using torque sensor; therefore, the method presented in [21] is adopted. The test rig is shown in Fig. 20(a). The prototype is clamped by a dividing dial and a beam is fixed to the rotor shaft. A weight is fixed on one side of beam in order to keep the force acting on the scale at any rotor position; moreover, the weight can reduce the influence of friction.

The cogging torque waveform can be obtained by the lever principle. Fig. 20(b) shows the comparison between the

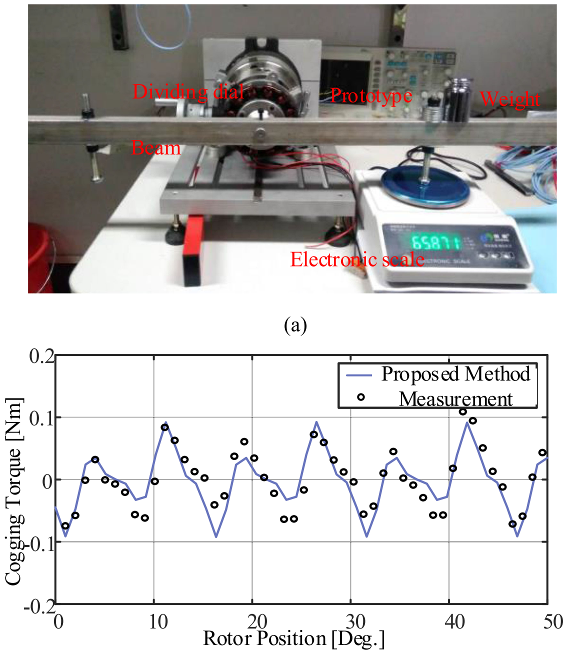

(b)

Fig. 20. Cogging torque result of slot opening with 5.8°. (a) Test rig. (b) Experimental result.

predicted proposed method and the measured cogging torque waveforms. An acceptable agreement has been achieved.

VII. CONCLUSION

The IPM machine has been emerging in various industrial applications, thanks to its wide constant power speed range. However, it has a critical problem with design and optimization process because of the long computation time if the calculation is done in FEM.

This paper proposed a hybrid method combining FEM and analytical method, which reduced the computation time remarkably while maintaining the high accuracy as that of the FE model. The hybrid results of MFD, back EMF, and the torque matched well with those of FEM, which confirmed the validity of the proposed model.

Moreover, the approach proposed in this paper can be regarded as an effective design and optimization tool for the IPM machine.

REFERENCES

[1] J. Dong, Y. Huang, L. Jin, and H. Lin, “Comparative study of surface-mounted and interior permanent-magnet motors for high-speed applications,” *IEEE Trans. Appl. Supercond.*, vol. 26, no. 4, pp. 1–4, Jun. 2016.

[2] Z. Yang, F. Shang, I. P. Brown, and M. Krishnamurthy, “Comparative study of interior permanent magnet, induction, and switched reluctance motor drives for EV and HEV applications,” *IEEE Trans. Transp. Electrific.*, vol. 1, no. 3, pp. 245–254, Oct. 2015.

[3] X. Liu, H. Chen, J. Zhao, and A. Belahcen, “Research on the performances and parameters of interior PMSM used for electric vehicles,” *IEEE Trans. Ind. Electron.*, vol. 63, no. 6, pp. 3533–3545, Jun. 2016.

[4] K.-H. Shin, J.-Y. Choi, and H.-W. Cho, “Characteristic analysis of interior permanent magnet synchronous machine with fractional slot concentrated winding considering nonlinear magnetic saturation,” *IEEE Trans. Appl. Supercond.*, vol. 26, no. 4, Jun. 2016, Art. no. 5200404.

[5] W. Zhu, B. Fahimi, and S. Pekarek, “A field reconstruction method for optimal excitation of permanent magnet synchronous machines,” *IEEE Trans. Energy Convers.*, vol. 21, no. 2, pp. 305–313, Jun. 2006.

[6] D. Torregrossa, B. Fahimi, F. Peyraut, and A. Miraoui, “Fast computation of electromagnetic vibrations in electrical machines via field reconstruction method and knowledge of mechanical impulse response,” *IEEE Trans. Ind. Electron.*, vol. 59, no. 2, pp. 839–847, Feb. 2012.

[7] D.-K. Lim, K.-P. Yi, S.Y. Jung, H.-K. Jung, and J.-S. Ro, “Optimal design of an interior permanent magnet synchronous motor by using a new surrogate-assisted multi-objective optimization,” *IEEE Trans. Magn.*, vol. 51, no. 11, pp. 1–4, Nov. 2015.

[8] P. Naderi, “Cage-rotor induction motor inter-turn short circuit fault detection with and without saturation effect by MEC model,” *ISA Trans.*, vol. 64, pp. 216–230, Sep. 2016.

[9] D. S. Mihic, M. V. Terzic, and S. N. Vukosavic, “A new nonlinear analytical model of the SRM with included multiphase coupling,” *IEEE Trans. Energy Convers.*, vol. 32, no. 4, pp. 1322–1334, Dec. 2017.

[10] Z. Q. Zhu, L. J. Wu, and Z. P. Xia, “An accurate subdomain model for magnetic field computation in slotted surface-mounted permanent-magnet machines,” *IEEE Trans. Magn.*, vol. 46, no. 4, pp. 1100–1115, Apr. 2010.

[11] L. Roubache, K. Boughrara, F. Dubas, and R. Ibtiouen, “Semi-Analytical modeling of spoke-type permanent-magnet machines considering the iron core relative permeability: Subdomain technique and Taylor polynomial,” *Prog. Electromagn. Res. B*, vol. 77, pp. 85–101, 2017.

[12] P. Liang, F. Chai, Y. Li, and Y. Pei, “Analytical prediction of magnetic field distribution in spoke-type permanent-magnet synchronous machines accounting for bridge saturation and magnet shape,” *IEEE Trans. Ind. Electron.*, vol. 64, no. 5, pp. 3479–3488, May 2017.

[13] L. Zhu, S. Z. Jiang, Z. Q. Zhu, and C. C. Chan, “Analytical modeling of open-circuit air-gap field distributions in multisegment and multilayer interior permanent-magnet machines,” *IEEE Trans. Magn.*, vol. 45, no. 8, pp. 3121–3130, Aug. 2009.

[14] H. Mirahki and M. Moallem, “Analytical prediction of cogging torque for interior permanent magnet synchronous machines,” *Prog. Electromagn. Res. M*, vol. 37, pp. 31–40, 2014.

[15] H. Chen, D. Li, R. Qu, Z. Zhu, and J. Li, “An improved analytical model for inductance calculation of interior permanent magnet machines,” *IEEE Trans. Magn.*, vol. 50, no. 6, Jun. 2014, Art. no. 7027108.

[16] L. J. Wu, Z. Q. Zhu, D. A. Staton, M. Popescu, and D. Hawkins, “Comparison of analytical models of cogging torque in surface-mounted PM machines,” *IEEE Trans. Ind. Electron.*, vol. 59, no. 6, pp. 2414–2425, Jun. 2012.

[17] D. Zarko, D. Ban, and T. A. Lipo, “Analytical solution for electromagnetic torque in surface permanent-magnet motors using conformal mapping,” *IEEE Trans. Magn.*, vol. 45, no. 7, pp. 2943–2954, Jul. 2009.

[18] D. C. J. Krop, E. A. Lomonova, and A. J. A. Vandenput, “Application of Schwarz-Christoffel mapping to permanent-magnet linear motor analysis,” *IEEE Trans. Magn.*, vol. 44, no. 3, pp. 352–359, Mar. 2008.

[19] T. Lubin, S. Mezani, and A. Rezzoug, “2-D exact analytical model for surface-mounted permanent-magnet motors with semi-closed slots,” *IEEE Trans. Magn.*, vol. 47, no. 2, pp. 479–492, Feb. 2011.

[20] J. D. Bisschop, P. Sergeant, A. Hemeida, H. Vansompel, and L. Dupré, “Analytical model for combined study of magnet demagnetization and eccentricity defects in axial flux permanent magnet synchronous machines,” *IEEE Trans. Magn.*, vol. 53, no. 9, pp. 1–12, Sep. 2017.

[21] Z. Q. Zhu, L. J. Wu, and M. L. M. Jamil, “Influence of pole and slot number combinations on cogging torque in permanent-magnet machines with static and rotating eccentricities,” *IEEE Trans. Ind. Appl.*, vol. 50, no. 5, pp. 3265–3277, Sep./Oct. 2014.

Baocheng Guo (S’14–M’18) received the B.E. degree in electrical engineering from the China University of Petroleum, Qingdao, China, in 2009, the M.E. degree in electrical engineering from the Harbin University of Science and Technology, Harbin, China, in 2014, and the Ph.D. degree in electrical engineering from Southeast University, Nanjing, China, in 2017.

He is currently a Postdoc Researcher with Southeast University. His research interests include the electromagnetic field computation and development of fast multiphysics models of electrical machines.

Yunkai Huang received the M.Sc. and Ph.D. degrees in electrical engineering from the Southeast University, Nanjing, China, in 2001 and 2007, respectively.

He is currently a Professor with the School of Electrical Engineering, Southeast University, Nanjing, China. His research interests include design and control of PM machine and high speed machine, its applications in domestic appliances, electric vehicles, railway traction, all-electric ships, more-electric aircraft, and wind power generation systems.

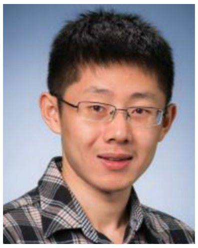

Fei Peng (S'15–M'16) received the B.S. and M.S. degrees in electrical engineering from Southeast University, Nanjing, China, in 2010 and 2012, respectively, and the Ph.D. degree in electrical and computer engineering from McMaster University, Hamilton, Ontario, Canada, in 2016.

After graduation, he worked as a postdoctoral fellow at the McMaster Institute for Automotive Research and Technology (MacAUTO), McMaster University. In December 2016, he joined the School of Electrical Engineering at Southeast University as an Assistant Professor. His research interests include optimal design and control of power converters, modeling and digital control of motor drives.

Jianning Dong (S'10–M'17) received the B.S. and Ph.D. degrees in electrical engineering from Southeast University, Nanjing, China, in 2010 and 2015, respectively.

Since 2016, he has been an Assistant Professor at the Delft University of Technology (TU Delft), Delft, The Netherlands. Before joining TU Delft, he was a Postdoc Researcher at McMaster Automotive Resource Centre (MARC), McMaster University, Hamilton, Ontario, Canada. His research interests are design, modeling, and control of electromechanical systems.